Impact of thermal boundary conductances on power dissipation and electrical breakdown of carbon nanotube network transistors

Man Prakash Gupta,[1] Liang Chen,[1] David Estrada,[2] Ashkan Behnam,[2] Eric Pop,[2,3] and Satish Kumar[1,a)]

[1]*G. W. Woodruff School of Mechanical Engineering, Georgia Institute of Technology, Atlanta, Georgia 30332, USA*
[2]*Micro and Nanotechnology Laboratory and Department of Electrical and Computer Engineering, University of Illinois, Urbana-Champaign, Illinois 61801, USA*
[3]*Beckman Institute, University of Illinois, Urbana-Champaign, Illinois 61801, USA*

We study the impact of thermal boundary conductance (TBC) at carbon nanotube (CNT)-substrate interfaces and CNT junctions on power dissipation and breakdown in CNT network based thin film transistors (CN-TFTs). Comparison of our results from an electro-thermal transport model of CN-TFTs to experimental measurements of power dissipation and temperature profiles allows us to estimate the average CNT-SiO$_2$ TBC as $g \sim 0.16 \, \mathrm{Wm}^{-1} \, \mathrm{K}^{-1}$ and the TBC at CNT junctions as $G_C \sim 2.4 \, \mathrm{pWK}^{-1}$. We find the peak power dissipation in CN-TFTs is more strongly correlated to the TBC of the CNT-substrate interface than to the TBC at CNT junctions. Molecular dynamics simulations of crossed CNT junctions also reveal that the top CNT is buckled over $\sim 30 \, \mathrm{nm}$ lengths, losing direct contact with the substrate and creating highly localized hot-spots. Our results provide new insights into CNT network properties which can be engineered to enhance performance of CN-TFTs for macro and flexible electronics applications. © *2012 American Institute of Physics*. [http://dx.doi.org/10.1063/1.4767920]

I. INTRODUCTION

Thin-film transistors (TFTs) are one of the most important components of macro-electronic circuits used in applications such as active matrix display drivers and X-ray image sensors.[1] The channel region of these TFTs is typically made of a-Si which has low carrier mobility ($<1 \, \mathrm{cm}^2 \, \mathrm{V}^{-1} \, \mathrm{s}^{-1}$) and involves high fabrication costs.[1] There has been a large research thrust towards replacing Si in these devices with new materials which offer greater mobility, improved flexibility, and high transparency along with simple, low cost, and high throughput fabrication.[1–9] Organic and carbon nanotube network based thin-film transistors (CN-TFTs) have been considered strong candidates in this regard, but CN-TFTs have the advantage over organic TFTs when it comes to performance and stability under ambient conditions.[10,11] Moreover, CN-TFTs have the potential to pave the way towards broader next generation macro-electronic devices and systems due to the exceptional electrical, mechanical, thermal, and optical properties of their building blocks, i.e., CNTs.[4–6,12,13] Among the most promising applications of these CN-TFTs are roll-up displays, large area sensors, radio frequency identification (RFID) tags, and antennas.[1,4,13–17]

However, there are many issues concerning the operational reliability of these devices which have not yet been explored. The structure of CNT junctions on substrate can become crucial in CN-TFTs as low thermal boundary conductances (TBCs) and high electrical resistances at these junctions can lead to junction temperatures hundreds of degrees

higher than the rest of the device, which will severely deteriorate the performance of CN-TFTs.[18–26] Moreover, active cooling may be impeded by low-thermal conductivity substrates (plastic, glass). As a result, self-heating during operation may lead to early breakdown of CN-TFTs and therefore presents a serious challenge to the device reliability particularly under high frequency and high bias operation.[27–29] Previous studies on electrical breakdown of single CNT transistors suggest that the TBCs at CNT interfaces play a major role in the power dissipation of CNTs.[30–35] However, the effect of TBCs on operating voltages, power dissipation, and reliability of CN-TFTs is not well understood.

In this work, we investigate power dissipation and network breakdown in CN-TFTs (schematic shown in Figure 1)
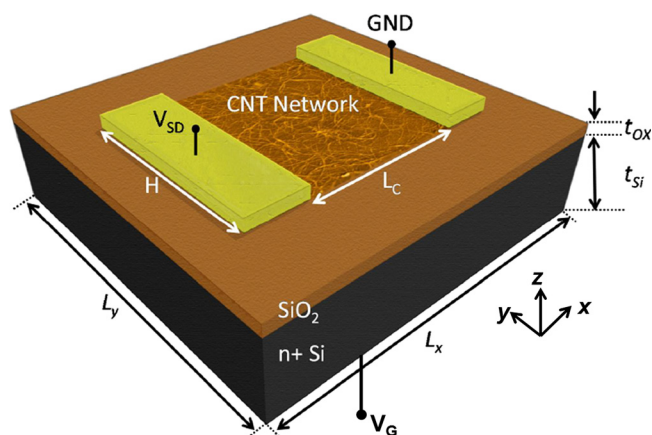

FIG. 1. Schematic/computational domain of a CN-TFT device. In our simulations, $L_x = 500 \, \mu m$, $L_y = 500 \, \mu m$, $L_C = 10 \, \mu m$, $H = 50 \, \mu m$, $t_{Si} = 500 \, \mu m$, $t_{OX} = 90 \, nm$.

a)Author to whom correspondence should be addressed. Electronic mail: satish.kumar@me.gatech.edu.

112, 124506-1

using a comprehensive approach which includes a coupled electro-thermal model of the network, molecular dynamics simulations of the junctions (Figure 2), and experimental transport and power dissipation data. Comparison of the measured CN-TFT power vs. source-to-drain voltage (P-V_{SD}) and temperature profiles with the corresponding numerical results (Figure 3) allows us to extract average TBCs at both CNT junctions and CNT-substrate interface simultaneously. The method followed here can be a valuable tool to extract interfacial thermal contact resistances for CNT networks on different substrates. We examine the temperature profile of the CNT network which may be very difficult to obtain directly from the experiments. We use our model to provide useful insights about the role of the two aforementioned TBCs in power dissipation and electrical breakdown of CN-TFT devices. Finally, we explore the effects of network morphology parameters such as network density and junction topology on network breakdown. Our analysis suggests that the CN-TFT performance and reliability can be significantly enhanced by improving the CNT-substrate interactions and optimizing the network morphology. Section II describes the numerical model and briefly summarizes the geometry and parameters of the fabricated devices which are further used in the numerical simulations, Sec. III validates the model against the experimental measurements, Sec. IV presents the results and discussion, and Sec. V concludes the paper.

II. METHODOLOGY

We employ a coupled electro-thermal model[36–38] to analyze the current, power, and temperature distribution in the device and simulate the network breakdown process with increasing V_{SD}. The model is based on the semi-classical drift-diffusion equations for charge transport in the CNT network and diffusive thermal transport equations for the CNT network, Si, and SiO$_2$ layers considering all interfacial contact resistances.

A. Electrical transport model

The electrical transport in CN-TFTs is described by Poisson's and drift-diffusion equations as follows:

$$\frac{d^2\Phi_i}{ds^2} + \frac{\rho_i}{\varepsilon} - \frac{(\Phi_i - V_G)}{\lambda^2} + \sum_{j \neq i} \frac{(\Phi_j - \Phi_i)}{\lambda_{ij}^2} = 0, \quad (1)$$

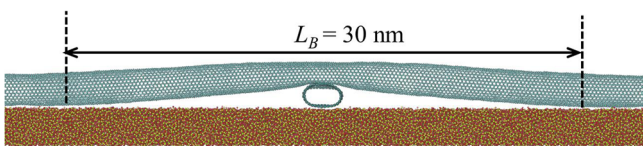$$\nabla \cdot J_{pi} + \sum_{j \neq i} C_{ij}^p (p_j - p_i) = 0, \quad (2)$$

FIG. 2. Equilibrated structure of the junction between two CNTs supported on a SiO$_2$ substrate, obtained from MD simulations. Using CNT diameter $d = 2$ nm we find $L_B \sim 30$ nm, which is the approximate length over which the top CNT loses thermal contact with the substrate.

$$\nabla \cdot J_{ni} + \sum_{j \neq i} C_{ij}^n (n_j - n_i) = 0, \quad (3)$$

$i = 1, 2, ...N$, where N is total number of tubes.

Here, Φ is the electrostatic potential, V_G is the gate voltage, ρ is the net charge density, ε is the permittivity of CNT, and s is the local axis along the length of an individual CNT. The term $-(\Phi - V_G)/\lambda^2$ in the Poisson equation is a parabolic approximation[37] which considers the gating effect. J is current density and p and n are hole and electron charge density, respectively. In the present case, n-doped Si acts as a back gate for the CN-TFTs (see Figure 1). λ is the effective screening length defined by $\lambda^2 = \varepsilon_{CNT} t_{OX} d / \varepsilon_{OX}$, where $\varepsilon_{CNT} \sim 5$ and $\varepsilon_{OX} \sim 3.9$ are the dielectric constants for the CNT network and gate oxide,[38] respectively. We estimate $\lambda \sim 27$ nm for a CNT film thickness equivalent to the CNT diameter value ($d \sim 2$ nm) and a gate oxide thickness of $t_{OX} \sim 90$ nm. The CNT-CNT electrostatic interaction is represented by the term $(\Phi_j - \Phi_i)/\lambda_{ij}^2$ when a node on CNT i intersects a node on CNT j, with a screening length λ_{ij}. The term $C_{ij}^n (n_j - n_i)$ in the continuity equation represents charge transfer between CNTs at the point of intersection. Here C_{ij}^n is the charge transfer coefficient;[39] higher values of C_{ij}^n imply better electrical contact at the junctions.

The network density ratio for metallic to semiconducting CNTs is considered to be 1:2. The gate voltage (V_G) is kept fixed at -15 V (on-state). The electrical contact resistance at the junction of a metallic (M) CNT and a semiconducting (S) CNT can be orders of magnitude higher than S-S or M-M junctions of CNTs.[26] C_{ij}^n is taken as zero for M-S junctions to account for very low contact conductance, and it is taken as 50 for S-S and M-M contacts. The drift-diffusion and Poisson equations are solved self-consistently to obtain the current-voltage distribution and the power dissipation in the CNT network. The power distribution is taken as an input for the subsequent thermal simulations to obtain the thermal profile in the device.

B. Thermal transport model

The thermal transport in the CNT-network, SiO$_2$ layer, and Si substrate is simulated using the diffusive energy transport equations as shown below:

$$\frac{d^2\theta_i}{ds^{*2}} + Bi_S(\theta_{OX} - \theta_i) + \sum_{\substack{\text{intersecting} \\ \text{tubes } j}} Bi_C(\theta_j - \theta_i) + \frac{d}{L_t} \frac{q_i'}{Q'} = 0,$$

$$(4)$$

$$\nabla^{*2}\theta_{OX} + \sum_{i=1}^{N_{tubes}} Bi_S \beta_v (\theta_i - \theta_{OX}) = 0, \quad (5)$$

$$\nabla^{*2}\theta_{Si} = 0. \quad (6)$$

Here, temperature (T) is non-dimensionalized as $\theta = (T - T_\infty)/(Q'dL_t/k_t)$. The asterisk symbol in the above equations indicates that the length variables are non-dimensionalized by the CNT diameter d. T_∞ is the ambient temperature, q_i' is the

volumetric Joule heating term within the CNT and Q' is a reference power per unit volume. θ_i, θ_{OX}, and θ_{Si} are non-dimensionalized temperatures of a section of the ith CNT, SiO_2, and Si, respectively. The third term in Eq. (4) represents thermal interaction between intersecting CNTs. In Eq. (5), the second term represents the thermal interaction between CNTs and oxide substrate. Equation (6) represents the diffusive thermal transport equation for the Si layer. Bi_C represents the non-dimensional TBC between intersecting CNTs. The non-dimensional parameter Bi_S represents the thermal interaction between a CNT and the substrate. The dimensionless parameters in these equations are defined as[22,37]

$$Bi_C = \frac{h_C P_C d^2}{k_t A}; \quad Bi_S = \frac{h_S P_S d^2}{k_t A}; \quad \beta_v = \alpha_v \left(\frac{A}{P_S}\right) \frac{k_t}{k_S}.$$

Here, h_C and h_S represent heat transfer coefficients at CNT-to-CNT and CNT-to-substrate contacts, respectively, P_C and P_S are the corresponding contact perimeters, k_t is the thermal conductivity of the CNT, k_S is the thermal conductivity of the substrate, and A is the CNT cross-sectional area. The parameter β_v characterizes the contact geometry and α_v is the contact area per unit volume of substrate. We use a constant temperature boundary condition, $T = 343$ K, applied at $z = 0$, i.e., at the bottom surface of Si substrate, while at the top surface of the SiO_2 layer, i.e., at $z = t_{Si} + t_{OX}$, a convective boundary condition is applied. The convective boundary condition can be expressed as $k_S dT/dz = h(T - T_\infty)$, where $T_\infty = 300$ K is the ambient temperature and h is the heat transfer coefficient at the top of the SiO_2 layer. The lateral boundaries at $x = 0$, $x = L_x$, $y = 0$, $y = L_y$ of the computational domain have been assumed to be thermally insulated.

C. Details of fabricated CN-TFTs

The computational domain of the CN-TFT (Figure 1) has been selected based on the experimental devices.[27] The details of the device fabrication and CNT-network morphology can be found in the previous studies.[27,40] Briefly, the CNT network is grown by chemical vapor deposition on SiO_2 ($t_{OX} = 90$ nm) supported by a highly n-doped Si substrate ($t_{Si} = 500\ \mu$m). The device is patterned by photolithography, and the contacts (Ti/Pd = 1/40 nm) are deposited by electron beam evaporation. The Si substrate acts as a back-gate and we set the gate-to-source voltage ($V_{GS} \leq -15$ V) such that both metallic and semiconducting tubes in the network are in the "on" state while V_{SD} is increased until network breakdown. Infrared (IR) thermal imaging of the device is performed with the bottom of Si substrate kept at a constant $T_0 = 70\ ^\circ$C (343 K), and the top surface is exposed to air to facilitate IR imaging and electrical breakdown due to oxidation. The CNT diameter distribution is obtained by atomic force microscopy (AFM), with an average diameter ~ 2 nm.[30,41]

The important dimensional parameters of the CN-TFT are channel length (L_c), channel width (H), average tube length (L_t), and CNT diameter (d) of 10 μm, 50 μm, 4 μm, and 2 nm, respectively (Figure 1). In real applications, CN-TFTs can be top-gated, and the substrates may be plastics or

glass, which may lead to different CNT-substrate TBC and junction morphology. The present analysis considers a range of TBCs which will include the possible TBC values at CNT junctions with different substrates. The device geometry, conductive properties of the substrate, and boundary conditions can be easily modified in the present model to consider the different applications of CN-TFTs.

D. Molecular dynamics simulations

The structure of CNT junctions in a CNT network can significantly affect the thermal transport between CNTs and between a CNT and the supporting substrate. We use molecular dynamics (MD) simulations to identify the junction structure and estimate the length (L_B) of the buckled segment of the top CNT which is not in direct contact with the SiO_2 layer (Figure 2). The adaptive intermolecular reactive empirical bond order potential (AIREBO) is used to describe C-C interactions in CNTs,[42] the Munetoh parameterization of the Tersoff potential to describe the Si-Si, O-O, and Si-O interactions,[43] and the Lennard-Jones potential to model the van der Waals interaction between CNT and SiO_2 atoms at the interface.[24,44] We first equilibrate the CNT-SiO_2 system using the canonical ensemble at 375 K for 300 ps and then sample the positions of each atom for 50 ps. In order to anchor the top CNT with the SiO_2 substrate, a very small force (0.02 Nm^{-1}) towards the substrate is applied on the top CNT during the first 100 ps simulation in NVT (constant volume and temperature ensemble), and then this force is removed. We observe $L_B \sim 30$ nm in the final structure (Figure 2). In most of our following electro-thermal transport analysis of the CN-TFT network, we consider that a 30 nm section of all top CNTs at the location of their junctions with other CNTs is not exchanging heat with the substrate directly.

III. VALIDATION

We find the simulation results to be in close agreement with experiments for both power (current) and temperature (Figure 3) at $g = 0.16$ Wm^{-1}K^{-1} ($Bi_S = 2 \times 10^{-4}$) and $G_C = 2.4$ pWK^{-1} ($Bi_C = 10^{-7}$). These values of TBCs are very close to the typically observed experimental and theoretical values in the literature.[23,24,27,30,32,45] Unlike previous studies, we find both g and G_C simultaneously by comparing the numerically estimated power dissipation and temperature profile in CN-TFTs against the experimental measurements. The power dissipation and thereby the temperature within the CNT network increases with increasing V_{SD} such that it eventually reaches the breakdown temperature of CNTs in air[30,46] ($\sim 600\ ^\circ$C). Some CNTs in the channel are likely to have higher current and power dissipation compared to the rest in the network, and therefore they experience earlier burnout due to excessive self-heating. As a result, percolation pathways change dynamically in the network as V_{SD} is increased further. This burnout process eventually results in a complete breakdown of the network along a random pattern between source and drain (Figure 3(a)). Our numerical simulations explain the experimental observations[27] of the breakdown process well. We consider 50 random networks
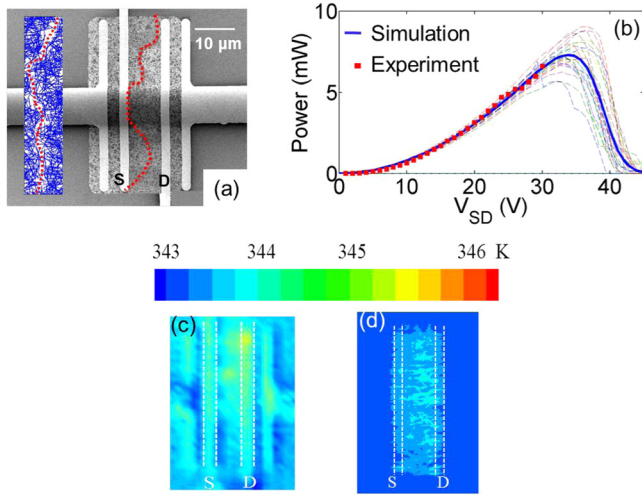
FIG. 3. (a) Comparison of random CNT network from simulations (left inset, channel region) to scanning electron microscopy (SEM) image of the CN-TFT used in experiments after the breakdown, respectively. The red dotted line shows the breakdown pattern of the network. (b) Comparison of computational results to experimental measurements of dissipated power vs. source-drain voltage (V_{SD}); the dark blue curve shows the statistical average of 50 random networks (dashed curves) obtained from the simulations. The power dissipation first increases with V_{SD}, then eventually drops to zero due to burning of CNTs which lead to complete network breakdown. (c),(d) Temperature profile at the SiO$_2$-Si interface obtained from infrared microscopy[27] and numerical simulation, respectively, for the device shown in (a).

to obtain the statistical average of current, power (dashed lines in Figure 3(b)), and the temperature distribution in a CN-TFT. The statistically averaged numerical results are in good agreement with the experimental measurement of power dissipation with increasing V_{SD} (Figure 3(b)) and the temperature profile at the SiO$_2$-Si interface obtained from infrared microscopy[27] (Figures 3(c) and 3(d)).

IV. RESULTS AND DISCUSSION

The experimental results based on IR measurements[27] revealed that the average temperature ($\sim$105 °C) in the channel region of CN-TFT near breakdown was well below the breakdown temperature[46] ($\sim$600 °C in air) of CNTs. Hand calculations[27] suggest that such a limited increase in temperature in the channel region could be attributed to highly localized nanometer-scale hot-spots at the CNT junctions, which cannot be captured by the IR microscopy with a resolution of $\sim$2 μm. We first perform detailed simulations to investigate the role of both CNT junction and CNT-substrate thermal conductances in the breakdown behavior (Sec.

IV A), and then we explore the effects of network density (Sec. IV B) and junction topology on the network breakdown (Sec. IV C).

A. Comparison of effects of TBCs (g and G_C) on power dissipation and thermal profile

Simulations reveal a very interesting feature about the role of junctions in heat dissipation which also supports the experimental observations. Results suggest that the typical junction TBC ($Bi_C = 10^{-7}$) is extremely low and a further decrease in Bi_C does not lead to any change in power and temperature distribution in the network. In other words, we find that for the typical value of the TBC at CNT junctions, the CNTs can be considered to be thermally non-interacting at their junctions. This particular result is consistent with the assumption that percolative thermal conduction in the network is typically absent.[47–49] Moreover, simulation results clearly show that even if we improve the junction conductance by two orders of magnitude ($Bi_C = 10^{-5}$, which may be practically improbable), it does not change the breakdown behavior of the CNT network significantly (Figure 4(a)). This extremely weak dependence of breakdown behavior on Bi_C can be attributed to very small junction area and the weak nature of thermal interaction at crossed CNT junctions.

We next turn to analyzing the effect of CNT-substrate thermal coupling (non-dimensional parameter Bi_S) on the power dissipation and the breakdown behavior of CN-TFTs. In order to study this dependence, we analyze the breakdown behavior of the network for Bi_C in the range of 10^{-7}–10^{-3} at different Bi_S values (10^{-6}–10^{-3}). The range selected here represents very poor to very good thermal contacts at CNT interfaces. The breakdown voltage increases significantly when Bi_S is increased (Figure 4(a)). The inset in Figure 4(a) shows the power variation in CN-TFT with V_{SD} at low Bi_S ($\sim$10^{-6}), and results suggest that the device fails before 10 V for all values of Bi_C in the range specified above. On the other hand, the device reaches peak power dissipation at $V_{SD} > 24$ V at Bi_S ($\sim$10^{-4}). It can be noted here that simply one order of magnitude increase in Bi_S can have a more positive impact on breakdown behavior than four orders of magnitude increase in Bi_C. These results clearly indicate that CNT junction TBC (Bi_C) plays only a secondary role to CNT-substrate TBC (Bi_S). Thus, the key to enhance the power density capability and device reliability lies in the improvement of CNT-substrate TBC. The two important characteristics of network breakdown, peak power (PP) and
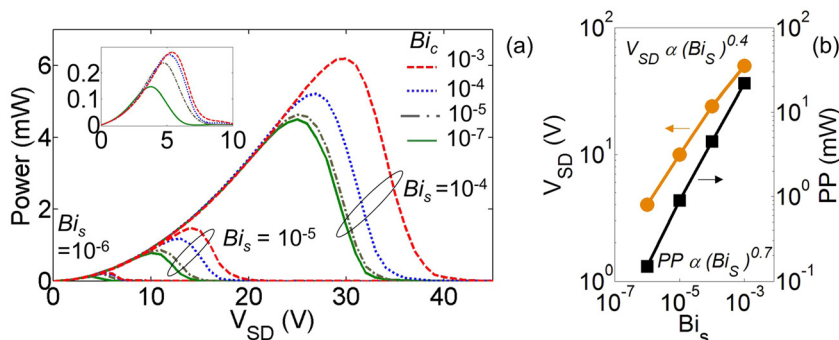

FIG. 4. (a) Variation of power dissipation in the CN-TFT vs. V_{SD} for different values of normalized thermal conductance at CNT junctions (Bi_C) and CNT-substrate interface (Bi_S); inset plot shows power vs. V_{SD} at $Bi_S = 10^{-6}$ for different values of $Bi_C = 10^{-7}$–10^{-3}. (b) Variation of peak power (PP, right axis) and V_{SD} (left axis) corresponding to peak power vs. Bi_S at $Bi_C = 10^{-7}$.
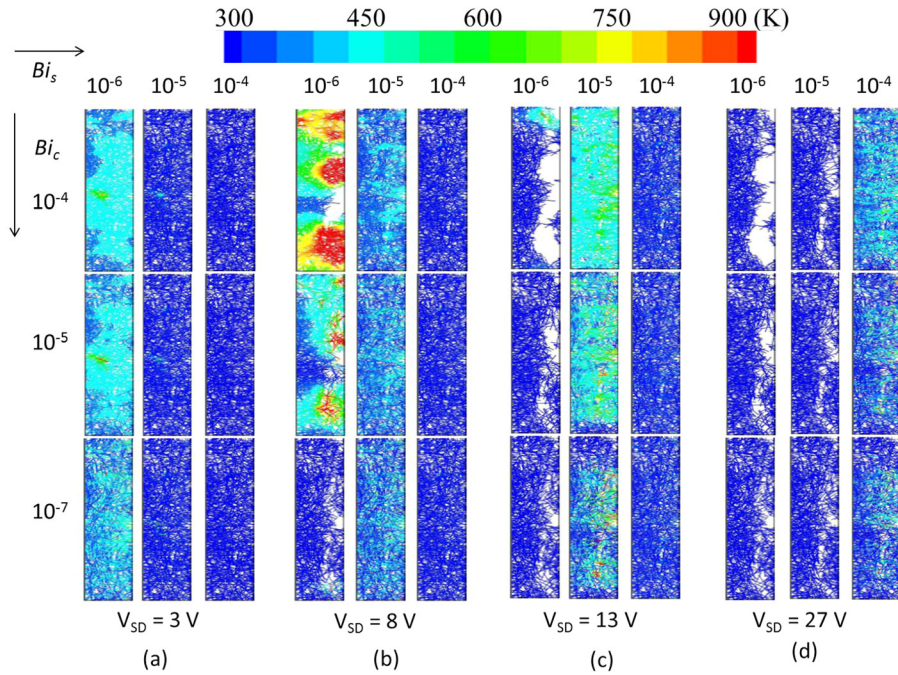
FIG. 5. Temperature profile in CNT networks for different values of Bi_C and Bi_S at (a) $V_{SD} = 3$ V, (b) $V_{SD} = 8$ V, (c) $V_{SD} = 13$ V, (d) $V_{SD} = 27$ V. Network density $\rho = 3.5$ CNTs/μm^2. In each case the current flows from left to right (source to drain) of the panels, respectively.

V_{SD} at peak power, both strongly depend on Bi_S and follow a power law relation with respect to Bi_S (Figure 4(b)).

The thermal profiles in a CNT network for different values of Bi_S and Bi_C at four different voltages (V_{SD}) are shown in Figure 5. It should be noted that the CNTs at high temperature are better able to transfer heat to other CNTs in the network at high Bi_C ($\sim 10^{-4}$). This leads to more uniform spreading of heat across the network, which in turn lowers the peak and average temperature of the network. At the same time, for low Bi_S ($\sim 10^{-6}$), the thermal interaction of CNTs with the substrate is negligible, and the temperature rises steeply with V_{SD} across the network. Subsequently, the temperature of a large cluster of CNTs in the network reaches the breakdown temperature simultaneously leading to big holes in the network (see left-top in Figures 5(b)–5(d)). In the case of low Bi_S ($\sim 10^{-6}$) and lower Bi_C ($< 10^{-4}$), the network breaks down at $V_{SD} < 10$ V along a curvy and random line because only fewer CNTs which form crucial percolative pathways burn due to excessive self-heating as they are not able to spread dissipated power to other CNTs or to substrate. On the other hand, if the CNT-substrate TBC is higher ($Bi_S \geq 10^{-5}$), the average temperature of the network is lowered due to increased power dissipation across the CNT-SiO$_2$ interface. This also translates into lower temperature at the junctions because heat can efficiently flow along the CNT-axis and then into the substrate at the locations where the CNT is in direct contact with the substrate.

As a result, breakdown occurs at higher V_{SD} (> 15 V) along a curvy and random breakdown pattern (see middle column in Figure 5(d)).

B. Network density

While our simulations suggest the TBC at CNT junctions may not have a large impact on CN-TFT device reliability for the typical value of CNT-substrate TBC observed in the experiments and discussed in this paper, these junctions are extremely important for charge transport across the channel. As the network density increases, the number of junctions and the percolation pathways for the electrical transport in the network also increases. This suggests that the network density directly affects the current and power dissipation in the channel and the breakdown of the network depends on the density. To analyze the impact of density variation on the breakdown process, we use the developed model to consider four different densities (ρ) for the same device geometry/configuration. TBCs are kept constant ($Bi_C = 10^{-7}, Bi_S = 10^{-4}$).

The results indicate that higher network density leads to higher power density in the network and consequently the breakdown occurs at lower V_{SD} (Figure 6(a)). For $\rho = 1.5$ CNTs/μm^2, power reaches a maximum of 1.7 mW at 30 V. For $\rho = 2.3$, 3.1, and 4.7 CNTs/μm^2, peak power $PP = 2.8$ mW, 3.4 mW, and 3.75 mW and the corresponding $V_{SD} = 27$,
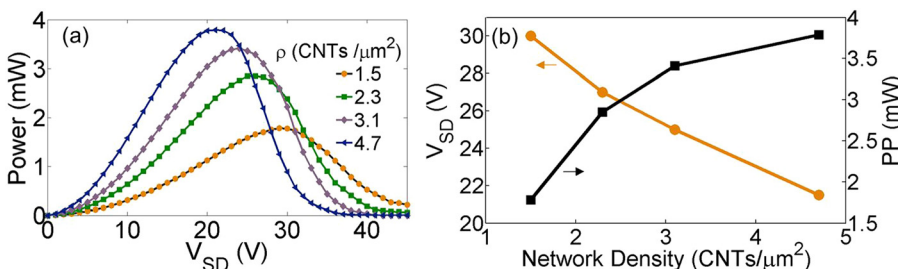

FIG. 6. (a) Power variation with V_{SD} for different network densities, until complete network breakdown is reached. Statistical average of 50 random networks has been considered for each density. (b) Peak power (PP, right axis) and V_{SD} (left axis) corresponding to peak power vs. network density.

25, and 21 V. Figure 6(b) shows that there is a clear trade-off between higher current and lower breakdown voltage with increasing network density. An optimum density of the network should be chosen to get sufficiently high current without the possibility of early breakdown under high bias operation.

C. Buckling at CNT junctions

Previous studies have shown that the fabrication process of CNT networks can affect the CNT network morphology, which will in turn influence the CN-TFT performance. For example, Timmermans *et al.*[40] show changes in the CNT network alignment, and CNT junction area, for similar network densities, would significantly affect the mobility, on/off ratio, and 1/f noise in CN-TFTs. Other studies have shown how the network conductivity can be tuned by controlling the network density and metallic-to-semiconducting CNT ratio.[50,51] Our model provides new insight into how network morphology influences device reliability by carefully considering the buckling length L_B (Figure 2), which can vary with network density due to increased CNT junction density. For some CNTs, the distance between two junctions along a CNT may be $L_B > 30$ nm as the network density increases. Consequently, at high densities, a large section of a single CNT within the network may not make direct contact with the substrate and is instead supported only by other CNTs. The non-contacting length of the top CNT depends on the diameter of top and bottom CNTs in addition to the distance between junctions and layout of lower CNTs. Results from MD simulations of a system shown in Figure 7(a) reveal that the total length of the buckled structure of the top CNT is 63 nm when two CNT junctions are separated by 25 nm. The non-contacting length increases with increasing CNT diameter. The large diameter

CNTs flatten due to a stronger vdW interaction with the surface[30,45] which will also have significant effects on the junction structure and non-contacting length. These sections of CNTs are likely locations of hot spots in the network which will strongly affect the breakdown characteristics.

We explore the effect of this non-contacting length at CNT junctions by considering two network densities, $\rho = 1.75$ CNTs/μm^2 and 3.5 CNTs/μm^2, and three cases of buckling length: $L_B = 30$ nm, 120 nm, and 200 nm. The average length of the CNTs in the network is $L_t = 4 \mu$m. The peak power dissipation in the network decreases by 50% and 70% corresponding to $\rho = 1.75$ and 3.5 CNTs/μm^2, respectively (Figure 7(b)), when the length of buckled sections is increased from $L_B = 30$ nm to 200 nm. V_{SD} corresponding to the peak power decreases by more than 33% when L_B is increased from 30 nm to 200 nm for both densities. The temperature of 10% of junctions increases by more than 150 °C at $V_{SD} = 15$ V as L_B increases from 30 nm to 200 nm for $\rho = 1.75$ CNTs/μm^2. The effect of L_B is even greater for the denser networks, as for $\rho = 3.5$ CNTs/μm^2 the temperature of at least 10% of junctions increases by more than 300 °C at the same $V_{SD} = 15$ V as L_B increases from 30 nm to 200 nm. This behavior is expected since a larger fraction of CNTs remain buckled due to the increased number of junctions per CNT. This result suggests that the network density ρ could be appropriately selected such that the distance between the junctions on a CNT is higher than the typical value of L_B to avoid early breakdown and enhanced reliability.

V. CONCLUSION

In summary, we have examined power dissipation and network breakdown in CN-TFTs through a comprehensive approach consisting of experiments, coupled electro-thermal model of the CN-TFT and molecular dynamics simulation of CNT junctions. We find that the breakdown characteristics remain invariant even if the TBC at junctions increases by two orders of magnitude from its typical value (~2.4 pWK^{-1}). We also observe that one order of magnitude increase in the CNT-substrate TBC from its typical value (~0.16 Wm^{-1} K^{-1}) will double the breakdown voltage and quadruple the maximum power dissipation capability of network. This analysis provides a useful insight into the role of CNT junctions in power dissipation. It implies that the CNT junctions are the likely locations of the hot spots not because of poor CNT-CNT thermal conductance but rather due to the absence of direct contact of buckled part of CNTs with the substrate at crossed CNT junctions. The denser network may adversely affect the device reliability as the higher percentage of CNTs may not be in direct contact with the substrate. Our analysis suggests that the CN-TFT performance can be greatly improved by engineering the CNT-substrate interactions and optimizing the network morphology.
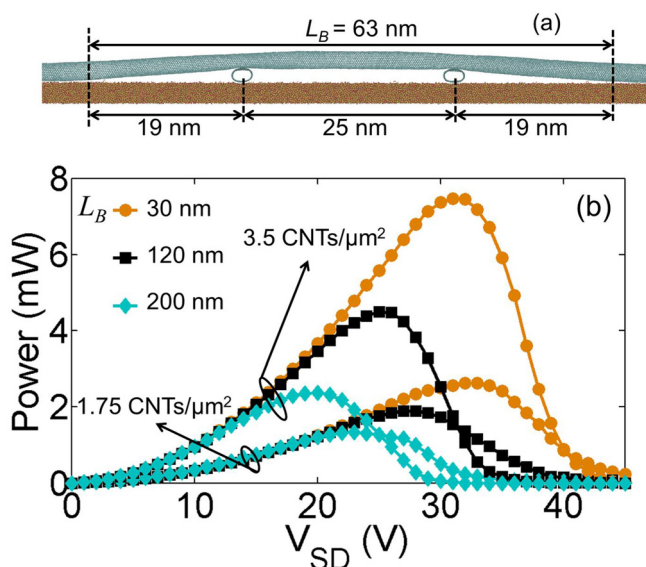

FIG. 7. (a) MD simulation result of a top CNT supported by two bottom CNTs spaced by 25 nm, leading to an apparently buckled structure of length $L_B = 63$ nm; CNT diameter $= 2$ nm, (b) Power vs. V_{SD} for two different network densities and different buckling lengths (L_B) at the junction for TBCs $Bi_C = 10^{-7}$ and $Bi_S = 2 \times 10^{-4}$. The effect of increased buckling length is larger for higher density.

[1]R. H. Reuss, B. R. Chalamala, A. Moussessian, M. G. Kane, A. Kumar, D. C. Zhang, J. A. Rogers, M. Hatalis, D. Temple, G. Moddel, B. J. Eliasson, M. J. Estes, J. Kunze, E. S. Handy, E. S. Harmon, D. B. Salzman, J. M. Woodall, M. A. Alam, J. Y. Murthy, S. C. Jacobsen, M. Olivier, D. Markus, P. M. Campbell, and E. Snow, Proc. IEEE **93**, 1239 (2005).

[2]M. Ha, Y. Xia, A. A. Green, W. Zhang, M. J. Renn, C. H. Kim, M. C. Hersam, and C. D. Frisbie, ACS Nano **4**, 4388 (2010).

[3]S. Kim, S. Kim, J. Park, S. Ju, and S. Mohammadi, ACS Nano **4**, 2994 (2010).

[4]Q. Cao and J. A. Rogers, Adv. Mater. **21**, 29 (2009).

[5]D.-M. Sun, M. Y. Timmermans, Y. Tian, A. G. Nasibulin, E. I. Kauppinen, S. Kishimoto, T. Mizutani, and Y. Ohno, Nat. Nanotechnol. **6**, 156 (2011).

[6]Q. Cao, H.-S. Kim, N. Pimparkar, J. P. Kulkarni, C. Wang, M. Shim, K. Roy, M. A. Alam, and J. A. Rogers, Nature (London) **454**, 495 (2008).

[7]M. C. LeMieux, M. Roberts, S. Barman, Y. W. Jin, J. M. Kim, and Z. Bao, Science **321**, 101 (2008).

[8]J. Opatkiewicz, M. C. LeMieux, and Z. Bao, ACS Nano **4**, 2975 (2010).

[9]J. P. Opatkiewicz, M. C. LeMieux, and Z. Bao, ACS Nano **4**, 1167 (2010).

[10]T. Sekitani, U. Zschieschang, H. Klauk, and T. Someya, Nat. Mater. **9**, 1015 (2010).

[11]X. Zhan, A. Facchetti, S. Barlow, T. J. Marks, M. A. Ratner, M. R. Wasielewski, and S. R. Marder, Adv. Mater. **23**, 268 (2011).

[12]K. Ryu, A. Badmaev, C. Wang, A. Lin, N. Patil, L. Gomez, A. Kumar, S. Mitra, H. S. P. Wong, and C. Zhou, Nano Lett. **9**, 189 (2008).

[13]G. Gruner, Anal. Bioanal. Chem. **384**, 322 (2006).

[14]D. Pribat and P. Bondavalli, J. Disp. Technol. **8**, 54 (2012).

[15]H. C. Lim, B. Schulkin, M. J. Pulickal, S. Liu, R. Petrova, G. Thomas, S. Wagner, K. Sidhu, and J. F. Federici, Sens. Actuators, A **119**, 332 (2005).

[16]C. Wang, J.-C. Chien, K. Takei, T. Takahashi, J. Nah, A. M. Niknejad, and A. Javey, Nano Lett. **12**, 1527 (2012).

[17]T. Takahashi, K. Takei, A. G. Gillies, R. S. Fearing, and A. Javey, Nano Lett. **11**, 5408 (2011).

[18]L. Hu, D. S. Hecht, and G. Grüner, Nano Lett. **4**, 2513 (2004).

[19]S. Kumar, J. Y. Murthy, and M. A. Alam, Phys. Rev. Lett. **95**, 066802 (2005).

[20]P. E. Lyons, S. De, F. Blighe, V. Nicolosi, L. F. C. Pereira, M. S. Ferreira, and J. N. Coleman, J. Appl. Phys. **104**, 044302 (2008).

[21]P. N. Nirmalraj, P. E. Lyons, S. De, J. N. Coleman, and J. J. Boland, Nano Lett. **9**, 3890 (2009).

[22]S. Kumar, M. A. Alam, and J. Y. Murthy, Appl. Phys. Lett. **90**, 104105 (2007).

[23]R. S. Prasher, X. J. Hu, Y. Chalopin, N. Mingo, K. Lofgreen, S. Volz, F. Cleri, and P. Keblinski, Phys. Rev. Lett. **102**, 105901 (2009).

[24]H. Zhong and J. R. Lukes, Phys. Rev. B **74**, 125403 (2006).

[25]J. Yang, S. Waltermire, Y. Chen, A. A. Zinn, T. T. Xu, and D. Li, Appl. Phys. Lett. **96**, 023109 (2010).

[26]M. S. Fuhrer, J. Nygård, L. Shih, M. Forero, Y.-G. Yoon, M. S. C. Mazzoni, H. J. Choi, J. Ihm, S. G. Louie, A. Zettl, and P. L. McEuen, Science **288**, 494 (2000).

[27]D. Estrada and E. Pop, Appl. Phys. Lett. **98**, 073102 (2011).

[28]S. Shekhar, M. Erementchouk, M. N. Leuenberger, and S. I. Khondaker, Appl. Phys. Lett. **98**, 243121 (2011).

[29]M. C. Strus, A. N. Chiaramonti, Y. L. Kim, Y. J. Jung, and R. R. Keller, Nanotechnology **22**, 265713 (2011).

[30]A. Liao, R. Alizadegan, Z.-Y. Ong, S. Dutta, F. Xiong, K. J. Hsia, and E. Pop, Phys. Rev. B **82**, 205406 (2010).

[31]E. Pop, Nanotechnology **19**, 295202 (2008).

[32]E. Pop, D. A. Mann, K. E. Goodson, and H. Dai, J. Appl. Phys. **101**, 093710 (2007).

[33]A. Javey, J. Guo, M. Paulsson, Q. Wang, D. Mann, M. Lundstrom, and H. Dai, Phys. Rev. Lett. **92**, 106804 (2004).

[34]H. Maune, H.-Y. Chiu, and M. Bockrath, Appl. Phys. Lett. **89**, 013109 (2006).

[35]R. V. Seidel, A. P. Graham, B. Rajasekharan, E. Unger, M. Liebau, G. S. Duesberg, F. Kreupl, and W. Hoenlein, J. Appl. Phys. **96**, 6694 (2004).

[36]S. Kumar, M. A. Alam, and J. Y. Murthy, J. Heat Transfer **129**, 500 (2007).

[37]S. Kumar, N. Pimparkar, J. Y. Murthy, and M. A. Alam, J. Appl. Phys. **109**, 014315 (2011).

[38]N. Pimparkar, Q. Cao, S. Kumar, J. Y. Murthy, J. Rogers, and M. A. Alam, IEEE Electron Device Lett. **28**, 157 (2007).

[39]C. Kocabas, N. Pimparkar, O. Yesilyurt, S. J. Kang, M. A. Alam, and J. A. Rogers, Nano Letters **7**, 1195 (2007).

[40]M. Timmermans, D. Estrada, A. Nasibulin, J. Wood, A. Behnam, D.-M. Sun, Y. Ohno, J. Lyding, A. Hassanien, E. Pop, and E. Kauppinen, Nano Res. **5**, 307 (2012).

[41]R. Alizadegan, A. Liao, F. Xiong, E. Pop, and K. Hsia, Nano Res. **5**, 235 (2012).

[42]S. J. Stuart, A. B. Tutein, and J. A. Harrison, J. Chem. Phys. **112**, 6472 (2000).

[43]S. Munetoh, T. Motooka, K. Moriguchi, and A. Shintani, Comput. Mater. Sci. **39**, 334 (2007).

[44]A. K. Rappe, C. J. Casewit, K. S. Colwell, W. A. Goddard, and W. M. Skiff, J. Am. Chem. Soc **114**, 10024 (1992).

[45]Z.-Y. Ong and E. Pop, Phys. Rev. B **81**, 155408 (2010).

[46]K. Hata, D. N. Futaba, K. Mizuno, T. Namai, M. Yumura, and S. Iijima, Science **306**, 1362 (2004).

[47]C.-W. Nan, G. Liu, Y. Lin, and M. Li, Appl. Phys. Lett. **85**, 3549 (2004).

[48]C. W. Nan, Z. Shi, and Y. Lin, Chem. Phys. Lett. **375**, 666 (2003).

[49]C.-W. Nan, R. Birringer, D. R. Clarke, and H. Gleiter, J. Appl. Phys. **81**, 6692 (1997).

[50]V. K. Sangwan, A. Behnam, V. W. Ballarotto, M. S. Fuhrer, A. Ural, and E. D. Williams, Appl. Phys. Lett. **97**, 043111 (2010).

[51]N. Rouhi, D. Jain, K. Zand, and P. J. Burke, Adv. Mater. **23**, 94 (2010).